System Development and Experimental Validation of a Long Range VNA-Based Channel Sounder

Mbugua, Allan Wainaina; Fan, Wei; Cai, Xuesong; Chen, Yun; Wang, Wei; Olesen, Kim; Pedersen, Gert Frølund

Published in:
IET Microwaves, Antennas & Propagation

DOI (link to publication from Publisher):
10.1049/iet-map.2019.0923

Publication date:
2020

Document Version
Accepted author manuscript, peer reviewed version

IET Journals
The Institution of Engineering and Technology

System Development and Experimental Validation of a Long Range VNA-Based Channel Sounder

ISSN 1751-8644
doi: 0000000000
www.ietdl.org

Allan Wainaina Mbugua[1,2], *Wei Fan*[2*], *Xuesong Cai*[2], *Yun Chen*[1], *Wei Wang*[3], *Kim Olesen*[2], *Gert Frølund Pedersen*[2]

[1] *Huawei Technologies Duesseldorf GmbH, Munich Research Center, Germany*
[2] *Antennas Propagation and Millimetre-wave Systems Section, Aalborg University, Aalborg, Denmark*
[3] *School of Information Engineering, Chang'an University,Xi'an, China*
* *E-mail: wfa@es.aau.dk*

Abstract:
In a wireless communication system, the radio propagation channel is a complicated component to characterize. Channel sounding equipment thus has to meet specific criteria to extract the desired channel parameters. In this paper, we outline the development and validation of a vector network analyzer (VNA) based channel sounder for the frequency range from 1 GHz to 50 GHz using radio-over-fiber (RoF) techniques. Three methods of de-embedding phase errors due to hardware impairments are demonstrated and validated via back-to-back measurements. The bidirectional scheme utilizing optical circulators is shown to have a superior performance over the two-branch unidirectional and the two-branch bidirectional schemes. Therefore, the bidirectional scheme utilizing optical circulators is proposed to achieve a long range ultra channel sounder based on the VNA.

1 Introduction

The demand for higher data rates and high radiolocalization accuracy in fifth generation (5G) and beyond networks have necessitated the use of ultra-wideband (UWB) systems [1–3]. This has led to the extensive research in the millimeter-wave (mm-wave) frequency bands where there is availability of large contiguous bandwidth [4–6]. System operation at mm-wave bands presents several opportunities, for example the small wavelength at mm-wave bands allows implementation of electrically large antenna arrays in compact form thus enabling state-of-the-art beamforming techniques [7]. Besides the mm-wave frequency bands, 5G networks are also expected to operate in centimeter-wave (cm-wave) frequency bands [8]. Channel modeling for 5G thus requires extensive characterization of radio channels over a wide frequency range.

Channel measurements over wide frequency ranges reported in the literature have been fundamental in validation and calibration of channel models [9]. With the rapid development of state-of-the-art channel emulation techniques, the measured channels can be replayed in controlled laboratory environments for device testing thus accelerating the integration of new features in 5G radios [10, 11]. Radio propagation channels are often characterized by high mobility of users, high user density and high diversity of materials with different constitutive parameters interacting with the propagating electromagnetic wave from the transmitter (Tx) to the receiver (Rx). Mobility of the Tx or Rx thus results in the Doppler effect on the propagating signal while the interaction of the electromagnetic wave with different materials in the propagation environment could result in a change of the polarization. In addition multipath rich environments results in different angle of arrival (AoA) of the multipath component (MPC)s. These phenomena present practical challenges on the channel sounding equipment which makes it very difficult to develop a one in all solution able to capture all the channel parameters [12].

Channel sounding approaches reported in the literature can generally be grouped in two major categories: time-domain based and frequency-domain based approaches. The time-domain approach enables tether-free channel sounding where the Tx and the Rx are not cable-connected and using of a wide instantaneous bandwidth thus capturing directional and dynamic radio channels [12–14]. Some of the techniques employed in time domain approach include the pseudo-random noise (PN) sequence based and the chirp based sounders. PN sequence based sounders employ a PN sequence known to both the Tx and Rx is transmitted and the channel impulse response (CIR) is recovered at the receiver by correlating the received signal with the transmitted signal [15]. This approach is widely adopted in the literature due the robustness of PN sequences to noise [16]. Another time-domain approach is the chirp based channel sounders e.g. the frequency modulated continuous wave (FMCW), where the chirp signal is recovered using matched filtering or a correlation based approach [17, 18]. State-of-the-art time-domain based channel sounders have the disadvantage that they are often too costly with complex synchronization and calibration mechanisms [19–21].

The frequency-domain approach to channel sounding has been widely adopted in the literature where the channel frequency response is recorded by performing a frequency sweep over a selected frequency band. The CIR is then obtained from the channel frequency response by performing an inverse Fourier transform. However, swept frequency techniques of channel sounding usually suffer from slow measurement time which is undesirable in time variant channels [22, 23]. In the literature, channel sounding in the frequency-domain is mainly performed using the vector network analyzer (VNA) which has less calibration and synchronization complexity as well lower hardware cost. In static radio channels, the VNA based channel sounders and virtual antenna arrays (VAA) are often used to obtain the spatio-temporal characteristics of the channel [24, 25]. However, the direct cable connection of the Tx and Rx to the VNA, significantly reduces the measurement distance and the dynamic range due to signal loss in coaxial cables especially at mm-wave frequencies. In addition, the measurement time when using the VNA scales up/down depending on the bandwidth selected for the frequency sweep, number of frequency points and the intermediate frequency (IF) bandwidth settings. Nonetheless, the VNA remains an attractive solution for channel measurements in indoor static scenarios and the distance limitation can be mitigated by the

use of frequency up-converters and down-converters or optical fiber cables [26–29].

The importance of channel sounder validation cannot be overstated. The accuracy of the measured CIR is dependent on the amplitude and phase stability of the channel sounder. Hardware impairments could result in variation of the amplitude response of the sounder thus causing spurious MPCs to be observed in the power delay profile (PDP) [30]. On the other hand, phase errors could undermine the accuracy of directional information obtained with the channel sounder especially when phased antenna arrays or VAA are employed in the measurement campaigns [31]. The non-idealities of the channel sounder hardware should therefore be identified and de-embedded from the measured CIR.

To enable inter-laboratory comparison of measurement data, several metrics and procedures are proposed in the literature for channel sounder validation. In [32], the dynamic range and the maximum measurable path loss are proposed as possible metrics and the extracted parameters compared with propagation theory. In [33, 34] channel sounder validation artifacts are developed to provide a common framework for comparison and evaluation of different channel sounders. In [35], two verification methods are proposed: *in-situ* and controlled condition verification. VNA based channel sounders have the advantage that the calibration procedures for the VNA is a well matured field [36]. After the VNA is calibrated appropriately, then only the additional components after the VNA test ports need to be characterized.

VNA channel sounders based on radio-over-fiber (RoF) techniques have the limitation that the phase of the signal propagating in the optical fiber is susceptible to variation stemming from temperature and strain gradients on the cable [37]. In [29], a phase correction bidirectional scheme for a RoF based VNA channel sounder using optical circulators is proposed and validated in back-to-back measurements, over the air channel measurements in an anechoic chamber and realistic propagation scenarios. The bidirectional scheme utilizing optical circulators is shown to achieve premium performance in correction of the phase errors due to temperature and strain gradients on the optical cable.

In this paper, three techniques of phase tracking for RoF based VNA channel sounders introduced in [26] (the two-branch unidirectional scheme, the two-branch bidirectional scheme and the bidirectional scheme using optical circulators) are comprehensively validated through back-to-back measurements for the frequency range from 1 GHz to 50 GHz. The work in [26] is further extended, and the major optical link parameters are investigated i.e. the optimum input power, the impact of the link gain variation over a wide bandwidth on the channel sounder's impulse response and the link budget for the three phase compensation schemes as well as the basic configuration.

The rest of the paper is organized as follows. Section 2 outlines the basic configuration of the optical link employed in the channel sounder, Section 3 describes the two-branch unidirectional phase correction scheme, Section 4 describes the two-branch bidirectional phase correction scheme, Section 5 outlines the bidirectional phase correction scheme using optical circulators and finally the conclusions are presented in Section 6.

2 Basic Configuration

The VNA is conventionally used to measure the scattering parameters (S-parameters) of a device under test (DUT). The DUT complex frequency response is then extracted from the measured S-parameters. An ideal linear time invariant (LTI) DUT is characterized by a flat frequency response over the bandwidth of operation. Radio channel measurements using the VNA consider static or slowly varying channels, thus the radio channel can be considered as a LTI DUT. The complex radio channel frequency response $h_{21}(f)$ is embedded in the measured $S_{21}(f)$ set as:

$$S_{21}(f) = h_{o1}(f)h_{21}(f) \quad (1)$$

where $h_{o1}(f)$ is the frequency response of the optical link as illustrated in Fig. 1. The frequency response of the channel $h_{21}(f)$, includes the effects of the Tx and Rx antenna i.e. the gain and the antenna pattern and over-the-air propagation channel.

2.1 Measurement Setup

The block diagram of the optical link employed in the RoF VNA based channel sounder is illustrated in Fig. 1 whereas the components used in the measurement setup are outlined in Table 1. The optical link is made of a laser and a photodetector with a frequency range of 1 GHz to 50 GHz and a 300 m single mode optical fiber cable. To characterize the link a two-port calibration procedure is

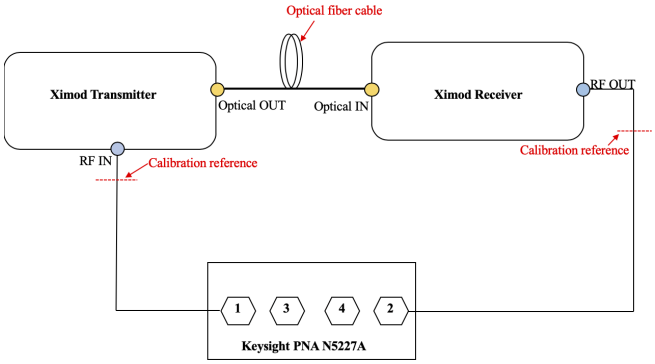

Fig. 1: Block diagram of the optical link employed in the RoF VNA based channel sounder

Table 1 Channel sounder components

Part	Name	Frequency
VNA	Keysight PNA N5227A	10 MHz - 67 GHz
RF amplifier	Cernex CBM26402520	26.5 GHz - 40 GHz
RF attenuator	Pasternack PE7090-20	DC - 40 GHz
Laser	Linear Photonics QMOD XMTQ-C-A-24	1550 nm
Photo detector	Linear Photonics QMOD XMRQ-C-A-24	1550 nm
Optical circulator	OZ optics FOC-12N-111-9/ 125-SSS-1550-55-SCASCASCA-1-1	1550 nm
Optical power splitter	JDS Uniphase FFC-CKH12B105-003	1550 nm

carried out to de-embed the frequency characteristics of the VNA test-port cables and to de-embed the VNA's systematic errors.

2.2 Measurement Parameters

2.2.1 Input 1 dB Compression: The optical link shown in Fig. 1 features integrated pre- and post-amplification stages in the Tx and Rx modules. The output power from the VNA test-port must thus be kept in the low distortion region to avoid driving the optical link into the 1 dB compression region. In the measurement setup shown in Fig. 1, the VNA output power from port 1 is progressively incremented from -80 dBm to 6 dBm in steps of 1 dBm. The VNA frequency sweep is then carried out from 1 GHz to 50 GHz with the number of frequency points set to 100001 and an IF bandwidth of 500 Hz. The laser is observed to go into compression for RF input power above -10 dBm as shown in Fig. 2. Subsequently VNA output power is set to -12 dBm.

2.2.2 Amplitude Response: Calibration of the amplitude response to compensate for the variation of the gain in the optical

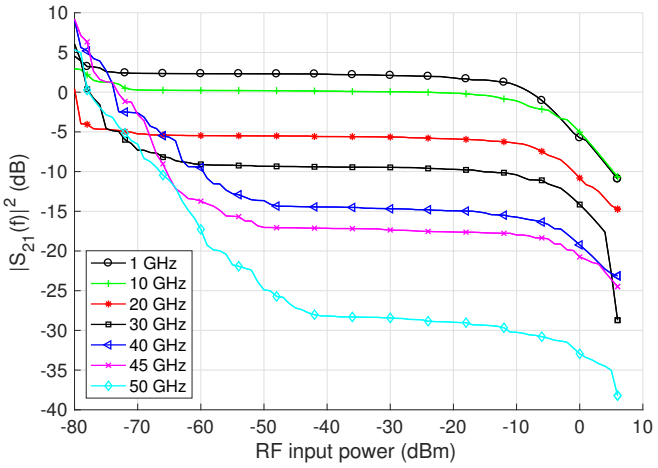

Fig. 2: Input 1 dB compression point of the optical link at selected frequencies

link is pivotal to achieve premium performance. The variation of the gain of the channel sounder in the operation band could result in spurious peaks being observed in the PDP of the measured channel. Due to hardware imperfections, the gain of the optical link varies significantly in the entire frequency range from 1 GHz to 50 GHz as illustrated in Fig. 3. The impulse response of the optical link before

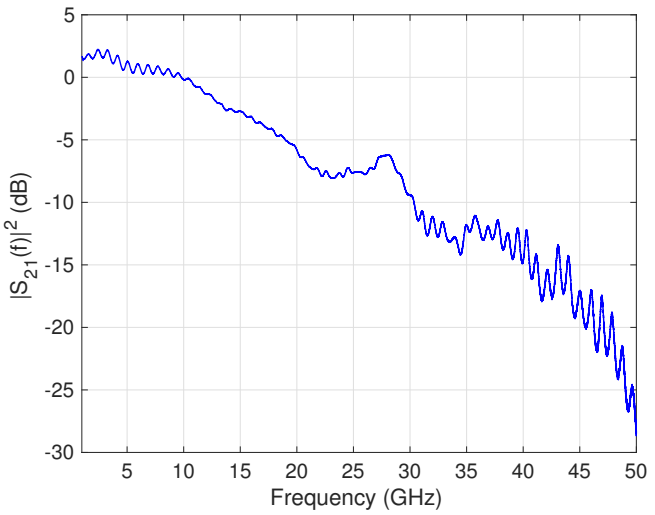

Fig. 3: Optical link gain at an input power of -12 dBm

normalization from 1 GHz to 50 GHz is shown in Fig. 4. The variation of the gain is seen to cause spurious peaks in the impulse response for the frequency range from 1 GHz to 50 GHz shown in Fig. 4a and the frequency range from 39 GHz to 40 GHz illustrated in Fig. 4b. The link gain is relatively flat from 14 GHz to 15 GHz compared to that of 39 GHz to 40 GHz which results in a spurious free impulse response as demonstrated in Fig. 4c. To prevent the optical link gain from being embedded in the measured channel response $h_{21}(f)$, a normalization procedure is carried out in back-to-back setup before measurements are conducted.

2.2.3 Phase Stability: The phase stability of the optical link is crucial when the channel sounder is used in measurement campaigns with VAA where movement of the optical cable is inevitable. The bending of the optical cable during measurement could be a potential source of phase errors. To verify the effect of cable bending during measurements on the phase, the setup shown in Fig. 1 is adopted. The optical cable bend diameter is varied from 60 cm to 20 cm as demonstrated in Fig. 5. The phase variation due to bending of the optical cable is shown in Fig. 6. The measurements are normalized with

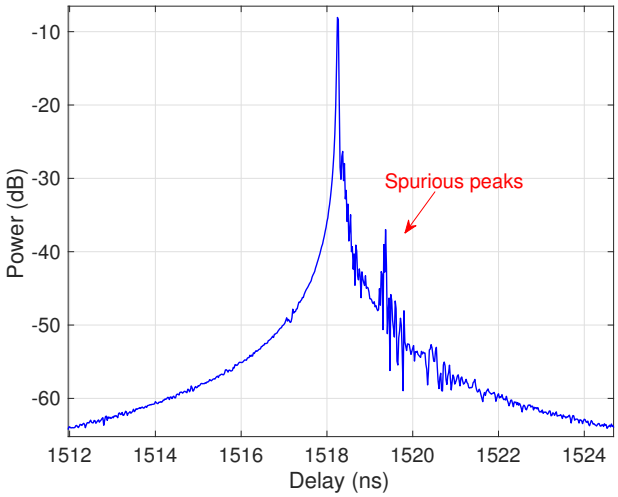

(a)

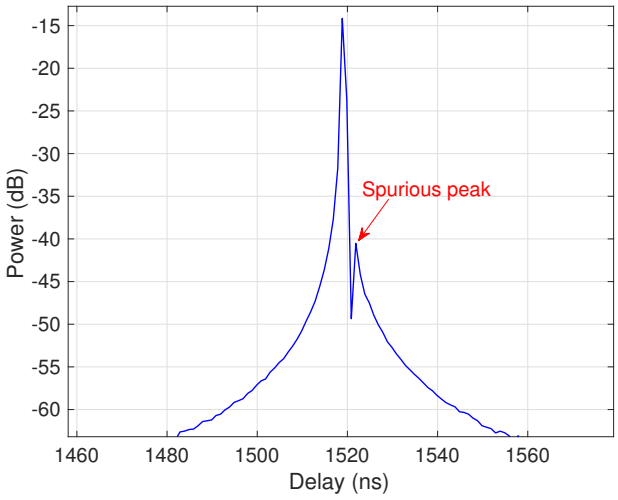

(b)

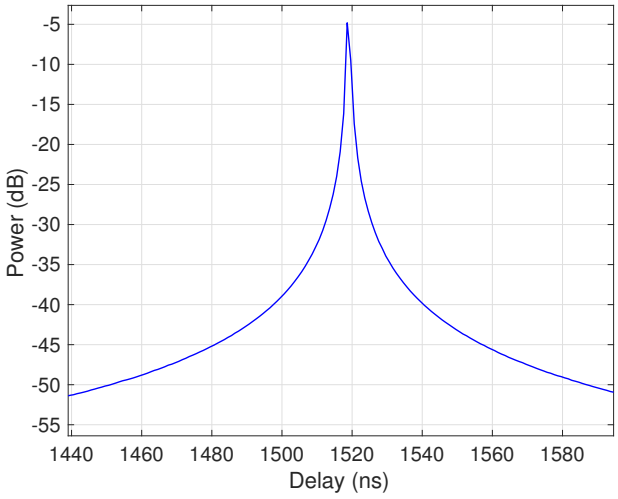

(c)

Fig. 4: Impulse response of the optical link before normalization at selected frequency bands illustrating the effect of amplitude variation. (a) 1 GHz to 50 GHz, (b) 39 GHz to 40 GHz, (c) 14 GHz to 15 GHz

respect to the 60 cm bend diameter. At 50 GHz, the phase is seen to vary by approximately 175 degrees. Bending the optical cable essentially results in changing its effective length. The change in effective

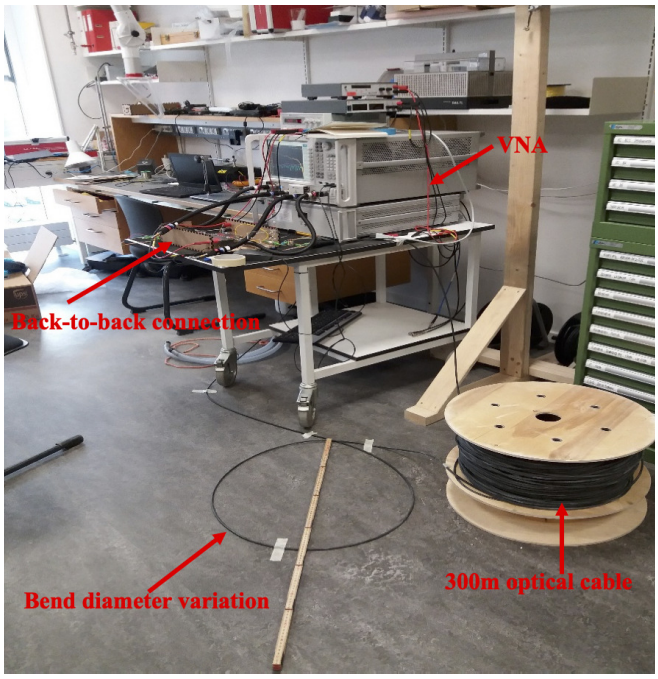

Fig. 5: Optical cable bending measurement setup

length Δl can be calculated as:

$$\Delta l = \frac{\theta}{360} \cdot \lambda \tag{2}$$

where θ is the change in phase in degrees and λ is the wavelength in meters. The change in the effective length of the optical cable is

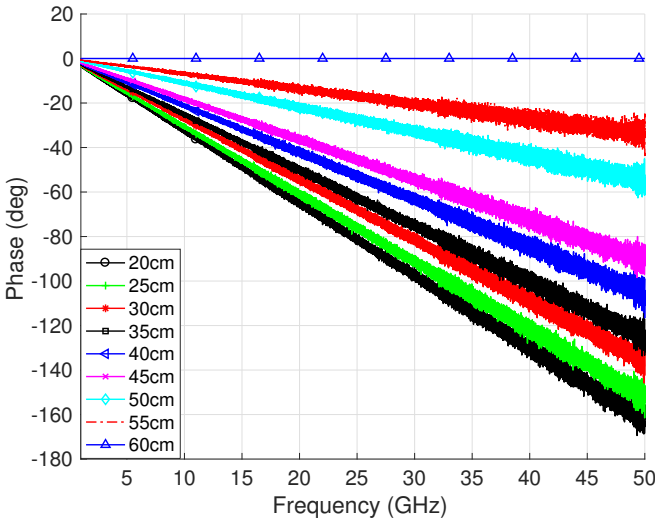

Fig. 6: Unwrapped phase with different cable bending diameters. All measurements are normalized to the 60 cm bend radius diameter

thus dependent on the bending which is rather stochastic in practical measurement scenarios. The system configuration shown in Fig. 1 is thus predominantly adopted in the literature to record power angular delay information using directive antennas [38]. However, to employ VAA in channel measurements, accuracy of phase information is critical.

2.3 Link Budget

Signal loss in the channel sounder components especially at mm-wave frequencies can lead to a significant reduction in the dynamic range. This effectively reduces the ability of the channel sounder to resolve weak MPCs as well as reducing the measurement range. A link budget analysis of the back-to-back connection at 30 GHz is carried out and shown in Fig. 7. The system has two limits. The

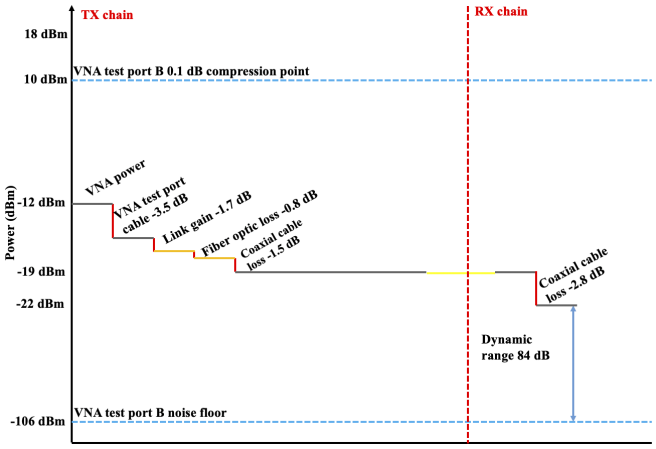

Fig. 7: Link budget of the optical link at 30 GHz

lower limit is the VNA's noise floor and is dependent on the frequency, where higher frequencies have a higher noise floor compared to lower frequencies. On the other hand, the upper limit is the input compression point of the VNA's receivers at the test ports. The VNA output power is fixed at -12 dBm as outlined in Section 2.2.1. At the end of the Tx chain the output power is approximately -19 dBm due to the signal loss in the coaxial cables and the optical link. In the Rx chain, the Keysight PNA N5227A has the option of direct access to the receiver ports, thus by-passing the directional coupler in the VNA's test-port (port 2 in Fig. 1). The directional coupler results in a 10 dB signal loss, thus in this setup we use the direct port access signal path to gain 10 dB in our link budget. The back-to-back connection including the Rx chain has a dynamic range of 84 dB.

3 Two-Branch Unidirectional Scheme

Phase coherent measurement using VNA-based channel sounders, are made on the premise that sounder's phase characteristics remain stable after calibration for the entire duration of the measurement. However, when using the optical link shown in Fig. 1, this cannot be guaranteed due to stochastic phase changes in the optical cable due to strain and temperature gradient. This limits the channel sounder to power measurements. A phase tracking mechanism is thus necessary for phase coherent channel measurements. The two-branch unidirectional scheme attains phase tracking by the use of two optical links and recording an extra set of S-parameters $S_{41}(f)$. The stochastic phase change on the optical cable can then be modeled by including an extra term $\Delta h_1(f)$ in (1).

$$S_{21}(f) = \Delta h_1(f) h_{o1}(f) h_{21}(f) \tag{3}$$

similarly, for the second link used for tracking the phase is recorded on the VNA as:

$$S_{41}(f) = \Delta h_2(f) h_{o2}(f) \tag{4}$$

where $\Delta h_2(f)$ and $h_{o2}(f)$ are the frequency response stemming from stochastic phase change and the frequency response of the second optical link, respectively. $h_{o1}(f)$ and $h_{o2}(f)$ can be calibrated out in a back-to-back measurement through a normalization procedure on the VNA, hence resulting in $h_{o1}(f) = h_{o2}(f) = 1$. Therefore, after an appropriate normalization procedure, (4) only contains the frequency response due to temperature and strain gradients on the optical cable, $\Delta h_2(f)$. For ideal optical cables of equal length and subject to the same temperature and strain gradient then the components $\Delta h_1(f)$ and $\Delta h_2(f)$ can be assumed to be equal,

therefore, the unwrapped phase of the channel frequency response $\angle h_{21}(f)$ can be obtained as:

$$\angle h_{21}(f) = \frac{\angle S_{21}(f)}{\angle S_{41}(f)} \tag{5}$$

3.1 Measurement Setup

The measurement setup for the two-branch unidirectional scheme is illustrated in Fig. 8. The system block diagram consists of an optical power splitter cascaded after the electrical to optical conversion stage. The 1-to-2 optical power splitter divides the signal into two before transmission on the optical fiber cable. The first link (forward link) is then connected to a Tx antenna while the second link (feedback link) which is used for phase tracking is maintained in a back-to-back connection in practical channel measurements as shown in Fig. 8.

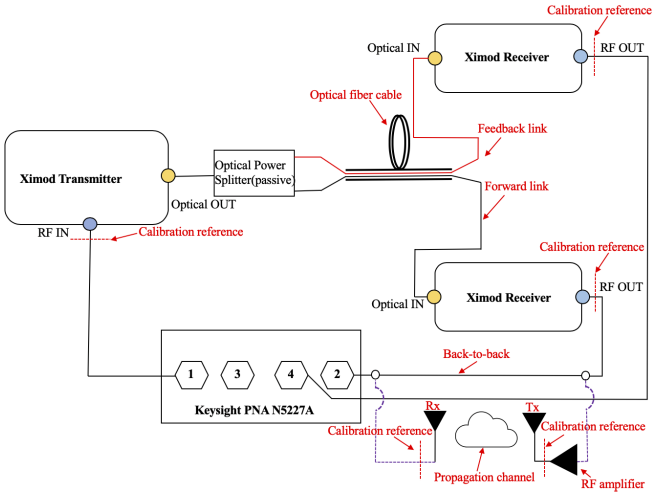

Fig. 8: Block diagram of the proposed two-branch unidirectional scheme

3.2 Phase Response

The phase response of the two-branch unidirectional scheme shown in Fig. 8 is experimentally validated using the measurement setup demonstrated in Fig. 5. The optical cable bend diameter is varied from 90 cm to 50 cm to record the effect of the cable bending on the phase of the signal. The measurements are then normalized with respect to the 90 cm bend diameter.

The phase variation of the signal on the first (forward link) and second (feedback link) optical cables are illustrated in Fig. 9a and Fig. 9b, respectively. The phase variation in the first optical cable is shown to vary by as much as 60° at 50 GHz due to the change in bend diameter. Similarly, for the second optical cable, the phase variation can be seen to vary by as much as 50° at 50 GHz. A phase variation difference of 10° can be observed at 50 GHz. This could be due to subtle differences in the strain gradient on the two cables which translates to different effective length change for the two cables. Although the two optical cables are housed by a common outer jacket, it is very difficult in practice to ensure that they experience exactly the same conditions thus $\Delta h_1(f)$ might not be exactly equal to $\Delta h_2(f)$. The phase correction of the two-branch unidirectional scheme is then carried out using (5). The corrected phase is illustrated in Fig. 9c. The difference in the effective length is then shown to result in residual errors with the maximum of 15° at 50 GHz. Although the phase correction is effective, the residual error observed in Fig. 9c might have an effect on the achieved accuracy of VAA algorithms.

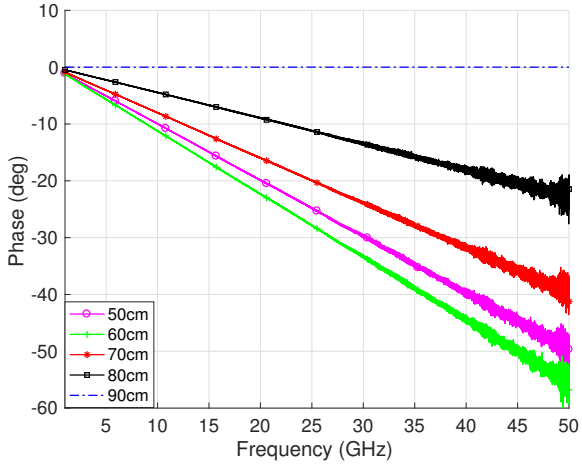

(a)

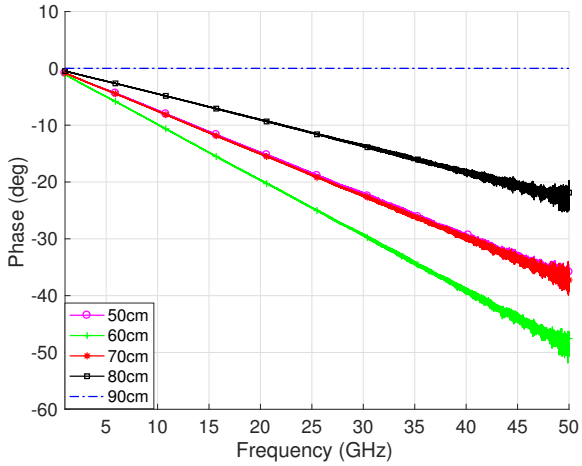

(b)

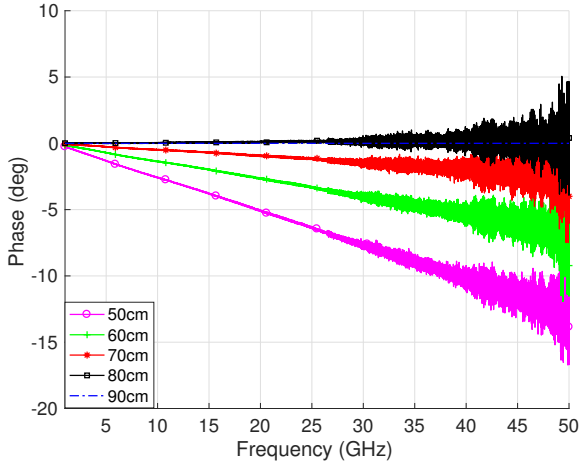

(c)

Fig. 9: Phase response of the two-branch unidirectional scheme due to cable bend diameter variation. (a) Forward link, (b) feedback link and (c) corrected phase

3.3 Link Budget

The link budget for the two-branch unidirectional scheme is illustrated in Fig. 10. The use of the optical power splitter results in an

RF signal power penalty of 6 dB. An RF power of -25 dBm is available after the optical to electrical conversion stage on both optical links. For the first optical link, where the Tx antenna is connected as illustrated in Fig. 8, an RF amplifier of with a gain of 40 dB and a noise figure of 6.2 dB is added before the antenna. In the back-to-back setup an RF attenuator of 10 dB is included to prevent the signal from the amplifier from driving the VNA receiver port into the compression region. Since the optical link has inbuilt pre and post-amplification stages with a noise figure of 18 dB at 30 GHz, the cascade of the pre- and post-amplification stages and the RF amplifier results in a noise figure of 18.3 dB at 30 GHz.

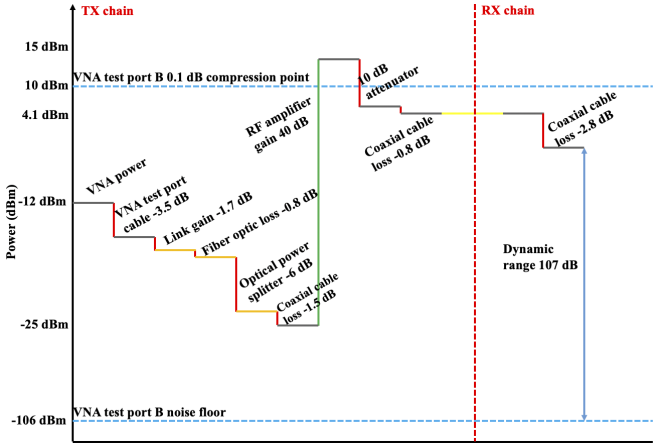

Fig. 10: Link budget of the two-branch unidirectional scheme at 30 GHz

4 Two-Branch Bidirectional Scheme

The system configuration shown in Fig. 8 employing (5) has the shortfall that it cannot be used in practical long-range channel sounding scenarios. This is because the second optical cable for the phase tracking signal is constantly connected to port 4 of the VNA during measurements. Since the two optical cable have to experience the same conditions, the physical separation of the Tx and Rx antenna is limited by the length of the coaxial cable from port 4 of the VNA to the output of the photo detector. Despite having a high back to back dynamic range of 107 dB as shown in Fig. 10, the two-branch unidirectional scheme is limited to measurements in short-range scenarios. The two-branch bidirectional scheme aims to extend the measurement range of the two-branch unidirectional scheme. This is attained by simply shifting the position of the optical power splitter to the end of the first optical cable and before the optical to electrical conversion stage as illustrated in Fig. 11. The phase tracking signal is then re-routed through a second optical cable to the VNA. After a back-to-back normalization procedure, then the phase of the tracking signal will have propagated twice the distance of the forward link. This assumption holds if and only if the two cables experience the same conditions. The phase correction in (5) is then modified as:

$$\angle h_{21}(f) = \frac{\angle S_{21}(f)}{0.5 \cdot \angle S_{41}(f)} \tag{6}$$

4.1 Measurement Setup

To characterize the phase response of the proposed scheme shown in Fig. 11, the optical cable bend diameter is varied from 90 cm to 50 cm to record the effect of the cable bending on the phase of the signal as demonstrated in Fig. 5. The phase error effects stemming from cable bending are then de-embedded using (6).

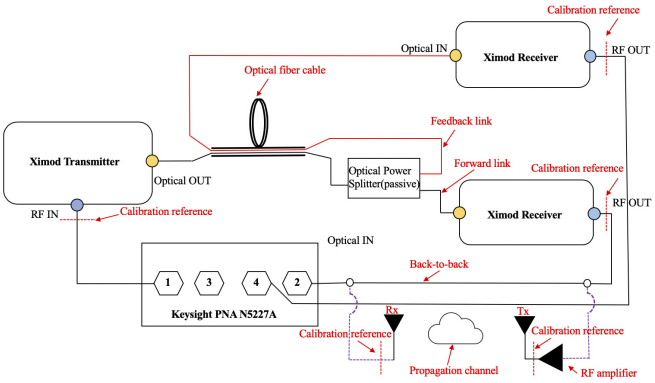

Fig. 11: Block diagram of the proposed two-branch bidirectional scheme

4.2 Phase Response

The unwrapped phase of the two-branch bidirectional scheme is shown in Fig. 12. The phase of the forward link is observed to vary by as much as 70° at 50 GHz as the cable bend diameter is varied from 90 cm to 50 cm as illustrated in Fig. 12a. For the feedback link, the phase is seen to vary by approximately twice as much as the phase in the forward link as shown in Fig. 12b. The phase correction is then carried out using (6). The phase error is corrected and maintained below 12° at 50 GHz as illustrated in Fig. 12c. The residual error is possibly due to the fact that in practical scenarios, there is a very low probability of the two optical cables experiencing exactly the same conditions i.e. the strain gradient. Thus the change in effective length is not equal at different bending diameters hence $\Delta h_1(f) \neq \Delta h_2(f)$ resulting in the differences observed in Fig. 12c.

4.3 Link Budget

The two-branch bidirectional scheme has the same link budget as the two-branch unidirectional scheme which is illustrated in Fig. 10. This is because the difference in the two configurations is the shift in the position of the optical power splitter.

5 Bidirectional Scheme

The residual error shown in Fig. 12c can be minimized by ensuring that $\Delta h_1(f) = \Delta h_2(f)$. A possible solution of ensuring that $\Delta h_1(f) = \Delta h_2(f)$ lies in utilizing the same optical cable for the forward and feedback links which mitigates the residual errors observed in Fig. 12c. Bidirectional transmission on the same optical fiber cable can be achieved by adopting optical circulators. The attractive features of optical circulators are low insertion loss, non-reciprocity and high isolation levels thus ensuring minimal interference of the forward and feedback link.

5.1 Measurement Setup

The system configuration is then modified as demonstrated in Fig. 13. The two 3-port non-polarization maintaining optical circulators have an isolation level of more than 40 dB and low insertion loss of 1 dB. Polarization-independent optical circulators are adopted in this case since the bending of the cable during the channel measurements inevitably results in a change of the light propagating in the optical cable. After the electrical to optical conversion stage, the optical signal propagates via port T of the optical circulator and goes into the optical cable from port 1 of the circulator. The optical cable is then cascaded with a second optical circulator where the signal goes in via port 1 and goes out via port R to the optical power splitter and finally to the photo detector. On the other hand, the feedback link goes from the optical power splitter into port T of the circulator and back into the optical cable via port 1. Finally, the feedback signal

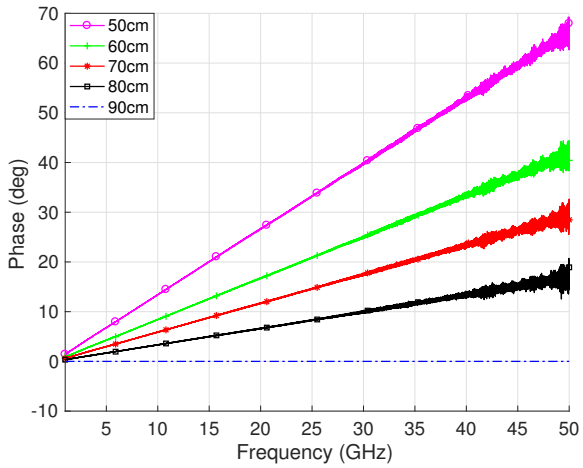

(a)

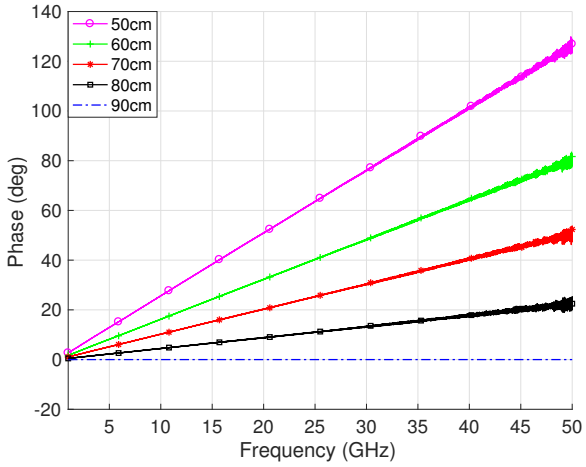

(b)

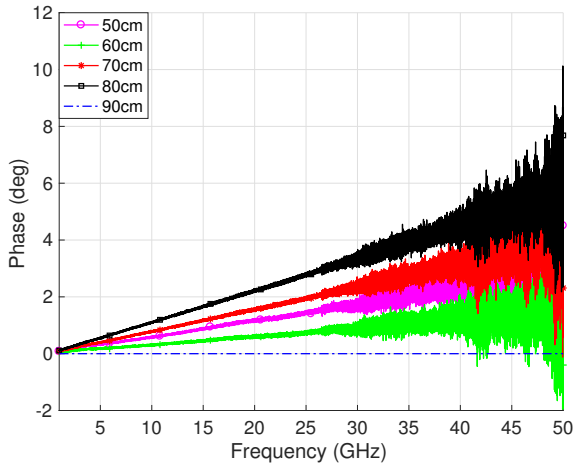

(c)

Fig. 12: Phase response of the two-branch bidirectional scheme due to cable bend diameter variation.(a) Forward link, (b) feedback link and (c) corrected phase

enters port 1 of the first circulator and goes into the photo-detector via from port R obtaining bidirectional link on a single optical cable.

The phase characterization of the bidirectional scheme is verified by mounting the optical cable on a turn-table used for practical VAA

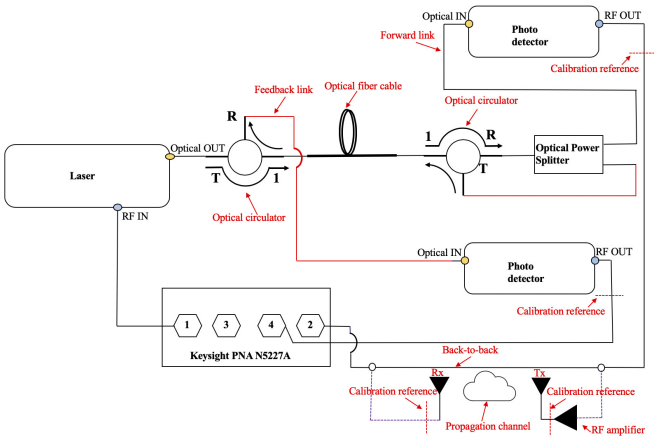

Fig. 13: Block diagram of the bidirectional scheme adopting optical circulators

measurements. The turn-table is rotated one full circle with a radius of 50 cm to mimic a virtual uniform circular array. The rotation is carried out using a resolution of 0.5° thus obtaining 720 spatial points.

5.2 Phase Response

The change of the phase due to the cable bending for the forward link is observed to be approximately 80° as shown in Fig. 14. In the feedback link the phase change is twice the phase change of forward link for each step as shown in Fig. 15. This is intuitively so because the transmission is on the same optical cable. The change in the phase is then corrected using (6) as illustrated in Fig. 16. The corrected phase has a residual error of 2° at 30 GHz and at 50 GHz the residual error is shown to be 14°. The residual error of 14° at 50 GHz is most likely due to the high noise figure at higher frequencies. In a high signal to noise ratio (SNR) regime, it is expected that the residual error can be maintained below 4°. The bidirectional scheme thus demonstrates superior performance over the two-branch unidirectional and two-branch bidirectional schemes over the entire frequency range from 1 GHz to 50 GHz.

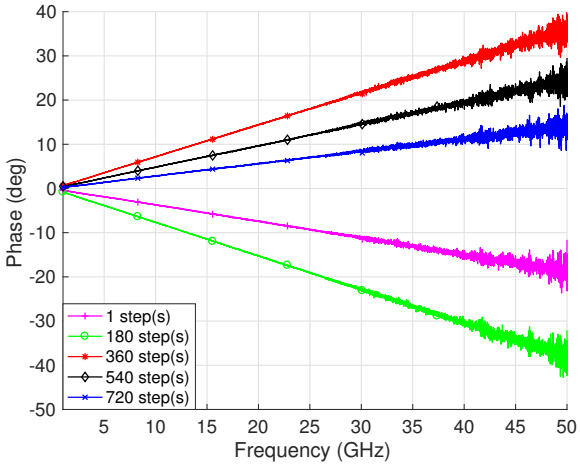

Fig. 14: Unwrapped phase response of the forward link at selected spatial points on the VAA

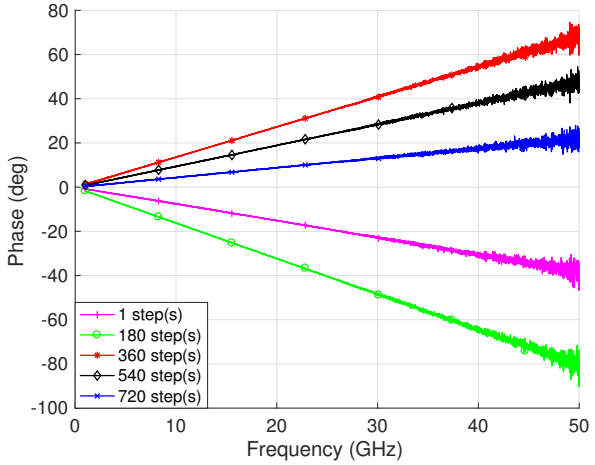

Fig. 15: Unwrapped phase response of the feedback link at selected spatial points on the VAA

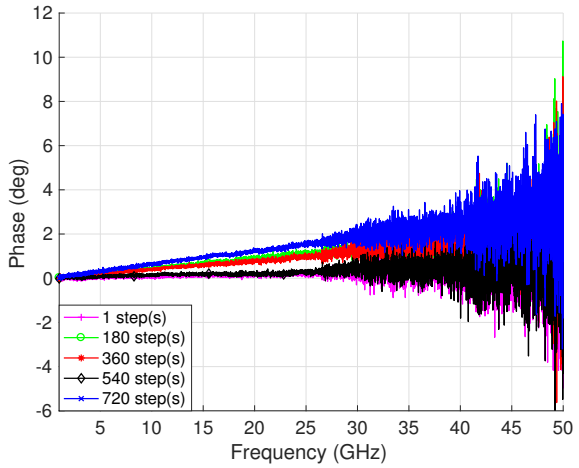

Fig. 16: Corrected phase response of the bidirectional scheme

5.3 Link Budget

The link budget of the bidirectional scheme is illustrated in 17. A back-to-back dynamic range of 112 dB is obtained at 30 GHz which enables long range channel measurements.

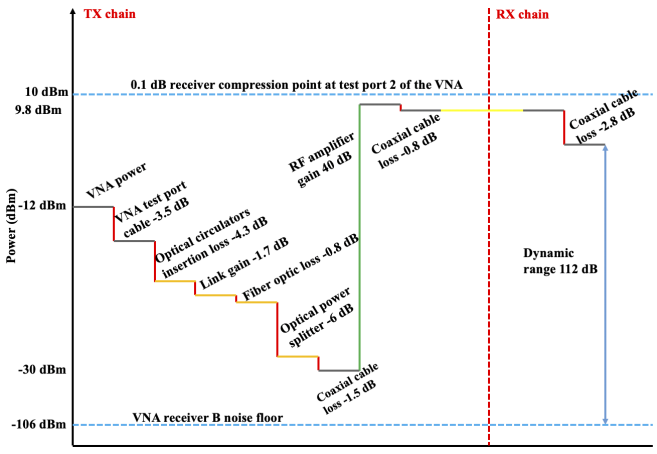

Fig. 17: Link budget of the bidirectional scheme at 30 GHz

6 Conclusion

In this paper, the system development and validation of an RoF VNA-based channel sounder is comprehensively presented. The power of the RF signal modulating the optical carrier is first determined to ensure the optical link operates in the low distortion region. The phase stability of the link is then evaluated for four configurations: the basic configuration, the two-branch unidirectional scheme, the two-branch bidirectional scheme and the bidirectional scheme employing optical circulators. The basic configuration shows a phase variation of about 175° which limits the VNA-based channel sounders using the optical link shown in Fig. 1 to power measurements. The two-branch unidirectional scheme achieved an improved phase accuracy over the basic configuration where the corrected phase has a residual error of 7° and 15° at 30 GHz and 50 GHz, respectively. Nonetheless, the two-branch scheme is limited to short range measurement scenarios. The two-branch bidirectional scheme achieves good phase correction with a residual error of approximately 4° and 10° at 30 GHz and 50 GHz, respectively while enabling long range measurements in contrast to the two-branch unidirectional scheme. The bidirectional scheme is shown to have a superior phase correction performance over the two-branch unidirectional and two-branch bidirectional schemes with a residual error of 2° and approximately 14° at 30 GHz and 50 GHz, respectively. This is due to the transmission on the same optical cable hence the phase change resulting from a change in effective length of the optical cable can be effectively compensated. The residual error at 50 GHz is most likely caused by the high noise figure and in a high SNR regime, it is expected that the residual error would be below 4°.

Acknowledgment

This work was supported by Huawei Technologies.

7 References

1 Guan, K., Ai, B., Peng, B., He, D., Li, G., Yang, J., et al.: 'Towards Realistic High-Speed Train Channels at 5G Millimeter-Wave Band—Part I: Paradigm, Significance Analysis, and Scenario Reconstruction', *IEEE Trans Veh Technol*, 2018, **67**, (10), pp. 9112–9128

2 Molisch, A.F.: 'Ultrawideband Propagation Channels-Theory, Measurement, and Modeling', *IEEE Trans Veh Technol*, 2005, **54**, (5), pp. 1528–1545

3 Witrisal, K., Meissner, P., Leitinger, E., Shen, Y., Gustafson, C., Tufvesson, F., et al.: 'High-Accuracy Localization for Assisted Living: 5G Systems Will Turn Multipath Channels from Foe to Friend', *IEEE Signal Process Mag*, 2016, **33**, (2), pp. 59–70

4 He, R., Ai, B., Stüber, G.L., Wang, G., Zhong, Z.: 'Geometrical-Based Modeling for Millimeter-Wave MIMO Mobile-to-Mobile Channels', *IEEE Trans Veh Technol*, 2018, **67**, (4), pp. 2848–2863

5 He, R., Schneider, C., Ai, B., Wang, G., Dupleich, D., Thomae, R., et al.: 'Propagation Channels of 5G Millimeter Wave Vehicle-to-Vehicle Communications: Recent Advances and Future Challenges', *IEEE Veh Technol Mag*, 2019, pp. 1–1

6 Zhao, X., Li, S., Wang, Q., Wang, M., Sun, S., Hong, W.: 'Channel Measurements, Modeling, Simulation and Validation at 32 GHz in Outdoor Microcells for 5G Radio Systems', *IEEE Access*, 2017, **5**, pp. 1062–1072

7 Ghosh, S., Sen, D.: 'An Inclusive Survey on Array Antenna Design for Millimeter-Wave Communications', *IEEE Access*, 2019, **7**, pp. 83137–83161

8 Kyösti, P., Lehtomäki, J., Medbo, J., Latva-aho, M.: 'Map-Based Channel Model for Evaluation of 5G Wireless Communication Systems', *IEEE Trans Antennas Propag*, 2017, **65**, (12), pp. 6491–6504

9 Fuschini, F., Häfner, S., Zoli, M., Müller, R., Vitucci, E.M., Dupleich, D., et al.: 'Analysis of In-Room Mm-Wave Propagation: Directional Channel Measurements and Ray Tracing Simulations', *J Infrared, Millimeter, Terahertz Waves*, 2017, **38**, (6), pp. 727–744

10 Fan, W., Carton, I., Kyösti, P., Pedersen, G.F.: 'Emulating Ray-Tracing Channels in Multiprobe Anechoic Chamber Setups for Virtual Drive Testing', *IEEE Trans Antennas Propag*, 2016, **64**, (2), pp. 730–739

11 Ji, Y., Fan, W., Pedersen, G.F., Wu, X.: 'On Channel Emulation Methods in Multiprobe Anechoic Chamber Setups for Over-the-Air Testing', *IEEE Trans Veh Technol*, 2018, **67**, (8), pp. 6740–6751

12 Nielsen, J.O., Fan, W., Eggers, P.C.F., Pedersen, G.F.: 'A Channel Sounder for Massive MIMO and MmWave Channels', *IEEE Commun Mag*, 2018, **56**, (12), pp. 67–73

13 Thoma, R.S., Hampicke, D., Richter, A., Sommerkorn, G., Schneider, A., Trautwein, U., et al.: 'Identification of Time-Variant Directional Mobile Radio Channels', *IEEE Trans Instrum Meas*, 2000, **49**, (2), pp. 357–364

14 Muller, R., Hafner, S., Dupleich, D., Luo, J., Schulz, E., Herrmann, R., et al. 'Ultra-Wideband Channel Sounder for Measurements at 70 GHz'. In: Proc. IEEE 81st Veh. Technol. Conf. (VTC Spring). (, 2015. pp. 1–5

15 Pirkl, R.J., Durgin, G.D.: 'Optimal sliding correlator channel sounder design', *IEEE Trans Wireless Commun*, 2008, **7**, (9), pp. 3488–3497

16 Mutagi, R.N.: 'Pseudo Noise Sequences for Engineers', *Electronics Communication Engineering Journal*, 1996, **8**, (2), pp. 79–87

17 Salous, S.: 'FMCW Channel Sounder With Digital Processing for Measuring the Coherence of Wideband HF Radio Links', *IEE Proceedings F - Communications, Radar and Signal Processing*, 1986, **133**, (5), pp. 456–462

18 Im, Y., Ali, M., Park, S.: 'Slow Modulation Behavior of the FMCW Radar for Wireless Channel Sounding Technology', *IEEE Trans Electromagn Compat*, 2014, **56**, (5), pp. 1229–1237

19 Bas, C.U., Wang, R., Sangodoyin, S., Psychoudakis, D., Henige, T., Monroe, R., et al.: 'Real-Time Millimeter-Wave MIMO Channel Sounder for Dynamic Directional Measurements', *IEEE Trans Veh Technol*, 2019, **68**, (9), pp. 8775–8789

20 MacCartney, G.R., Rappaport, T.S.: 'A Flexible Millimeter-Wave Channel Sounder With Absolute Timing', *IEEE J Sel Areas Commun*, 2017, **35**, (6), pp. 1402–1418

21 Papazian, P.B., Gentile, C., Remley, K.A., Senic, J., Golmie, N.: 'A Radio Channel Sounder for Mobile Millimeter-Wave Communications: System Implementation and Measurement Assessment', *IEEE Trans Microw Theory Techn*, 2016, **64**, (9), pp. 2924–2932

22 Salous, S., Feeney, S.M., Raimundo, X., Cheema, A.A.: 'Wideband MIMO Channel Sounder for Radio Measurements in the 60 GHz Band', *IEEE Trans Wireless Commun*, 2016, **15**, (4), pp. 2825–2832

23 Zetik, R., Kmec, M., Sachs, J., Thomä, R.S.: 'Real-Time MIMO Channel Sounder for Emulation of Distributed Ultrawideband Systems', *Int J Antennas Propag*, 2014, **2014**, pp. 317683

24 Mbugua, A.W., Fan, W., Ji, Y., Pedersen, G.F.: 'Millimeter Wave Multi-User Performance Evaluation Based on Measured Channels With Virtual Antenna Array Channel Sounder', *IEEE Access*, 2018, **6**, pp. 12318–12326

25 Medbo, J., Asplund, H., Berg, J.. '60 GHz Channel Directional Characterization Using Extreme Size Virtual Antenna Array'. In: Proc. IEEE 26th Annu. Int. Symp. Pers. Indoor, Mobile Radio Commun. (PIMRC). (, 2015. pp. 176–180

26 Fan, W., Mbugua, A.W., Cai, X., Olesen, K. 'Development and Experimental Validation of an Ultra-Wideband Channel Sounder'. In: Proc. 13th Eur. Conf. Antennas Propag. (EuCAP). (, 2019. pp. 1–5

27 Hejselbaek, J., Ji, Y., Fan, W., Pedersen, G.F.: 'Channel Sounding System for MM-Wave Bands and Characterization of Indoor Propagation at 28 GHz', *Int J Wireless Inf Netw*, 2017, **24**, (3), pp. 204–216

28 Liya, B.N., Michelson, D.G. 'Characterization of Multipath Persistence in Device-to-Device Scenarios at 30 GHz'. In: Proc. IEEE Globecom Workshops (GC Wkshps). (, 2016. pp. 1–6

29 Mbugua, A.W., Fan, W., Olesen, K., Cai, X., Pedersen, G.F.: 'Phase-Compensated Optical Fiber-Based Ultrawideband Channel Sounder', *IEEE Trans Microw Theory Techn*, 2019, pp. 1–12

30 Li, J., Zhao, Y., Tao, C., Ai, B.: 'System Design and Calibration for Wideband Channel Sounding With Multiple Frequency Bands', *IEEE Access*, 2017, **5**, pp. 781–793

31 Caudill, D., Papazian, P.B., Gentile, C., Chuang, J., Golmie, N.: 'Omnidirectional Channel Sounder With Phased-ArrayAntennas for 5G Mobile Communications', *IEEE Trans Microw Theory Techn*, 2019, **67**, (7), pp. 2936–2945

32 Peter, M., Weiler, R.J., Keusgen, W., Eichler, T., Kottkamp, M., Nähring, A. 'Characterization of Mm-wave Channel Sounders up to W-Band and Validation of Measurement Results'. In: Proc. 10th Eur. Conf. Antennas Propag. (EuCAP). (, 2016. pp. 1–5

33 Dortmans, J.N.H., Quimby, J.T., Remley, K.A., Williams, D.F., Senic, J., Sun, R.: 'Design of a Portable Verification Artifact for Millimeter-Wave-Frequency Channel Sounders', *IEEE Trans Antennas Propag*, 2019, **67**, (9), pp. 6149–6158

34 Quimby, J., Michelson, D.G., Bennai, M., Remley, K.A., Kast, J., Weiss, A. 'Inter-laboratory Millimeter-Wave Channel Sounder Verification'. In: Proc. 13th Eur. Conf. Antennas Propag. (EuCAP). (, 2019. pp. 1–5

35 Remley, K.A., Gentile, C., Zajic, A., Quimby, J.T. 'Methods for Channel Sounder Measurement Verification'. In: Proc. IEEE 86th Veh. Technol. Conf. (VTC-Fall). (, 2017. pp. 1–4

36 Lewandowski, A., Wiatr, W., Gu, D., Orloff, N.D., Booth, J.: 'A Multireflect-Thru Method of Vector Network Analyzer Calibration', *IEEE Trans Microw Theory Techn*, 2017, **65**, (3), pp. 905–915

37 Roman, J.E., Frankel, M.Y., Williams, K.J., Esman, R.D. 'Temperature and Strain Gradient Effects on Optical Fiber Cables for Phased-Array Antennas'. In: Proc. Opt. Fiber Commun. Conf. (, 1997. p. 171

38 Haneda, K., Nguyen, S.L.H., Järveläinen, J., Putkonen, J. 'Estimating the Omni-Directional Pathloss From Directional Channel Sounding'. In: Proc. 10th Eur. Conf. Antennas Propag. (EuCAP). (, 2016. pp. 1–5